Optical and EPR study of the Ce^{3+} luminescent centers in the Lu_2SiO_5 :Ce single crystalline films

Valentyn Laguta[1*], Martin Nikl[1], Mykhailo Trubitsyn[1], Vitalii Gorbenko[2], Tetiana Zorenko[2], Sandra Witkiewicz-Lukaszek[2], Alexander Fedorov[4], Yuriy Zorenko[2,3*]

[1]*Institute of Physics Academy of Science of Czech Republic,*

*Cukrovarnická 10,162 00 Prague 6, Czech Republic;*laguta@fzu.cz*

[2]*Department of Physics, Kazimierz Wielki University in Bydgoszcz,*

*Powstańców Wielkopolskich str., 2, 85-090 Bydgoszcz, Poland, *zorenko@ukw.edu.pl*

[3]*Oncology Centers in Bydgoszcz, I. Romanowska str., 2, 85-796 Bydgoszcz, Poland*

[4]*SSI Institute for Single Crystals, National Academy of Sciences of Ukraine, av. Nauki 60, 61178 Kharkiv, Ukraine*

Abstract. The work presents the results of optical and EPR investigations of Ce^{3+} incorporation into Lu_2SiO_5 single crystalline films (LSO:Ce SCFs), grown using the liquid phase epitaxy method. It also examines the conversion of Ce valence state as a result of the LSO:Ce SCF thermal treatment in reducing and oxygen-rich atmospheres. The EPR study revealed the presence of only one type of Ce^{3+} center (Ce1), corresponding to the localization of Ce^{3+} ions in sevenfold coordinated positions within the Lu_2SiO_5 host. No spectra of Ce2 centers (sixfold coordinated Ce^{3+} positions) were detected in the LSO:Ce SCF films, indicating their negligibly small concentration. High-temperature annealing of the as grown films in air reduces the concentration of Ce^{3+} ions to a level undetectable by EPR, due to the $Ce^{3+} \rightarrow Ce^{4+}$ conversion. In contrast, thermal treatment in a 95%N_2 + 5%H_2 reducing atmosphere results in the opposite $Ce^{4+} \rightarrow Ce^{3+}$ conversion, substantially increasing the concentration of Ce^{3+}. The oxidation/reduction treatment and Ce^{3+}/Ce^{4+} valence state changing lead to notable variations in the scintillation light yield and decay kinetics of the LSO:Ce SCFs, offering a method to tune their scintillation figure of merit.

Keywords: Lu_2SiO_5 orthosilicates, Ce^{3+} dopant, liquid phase epitaxy, single crystalline films, absorption, luminescence, scintillation, EPR.

1. Introduction

Scintillating materials, used for the detection of high-energy photons and particles, are continually developed to meet the demands of current and emerging applications. This research area encompasses a wide variety of material systems (see [1–3] and references therein). Novel high-performance scintillators are typically explored among cerium and praseodymium doped complex oxides due to their fast scintillation response driven by 5d–4f transitions in Ce^{3+} and Pr^{3+} ions, as well as their high efficiency and favourable mechanical and chemical properties.

Over the past decade, several new mixed-oxide-based scintillation materials with superior light yield (LY), and excellent energy resolution have been developed [2, 4, 5]. In particular, Ce-doped Lu_2SiO_5 (LSO), $(Lu,Y)_2SiO_5$ (LYSO), and $(Lu,Gd)_2SiO_5$ (LGSO) orthosilicates now represent a class of highly efficient and fast scintillating materialsn[1, 2, 4, 5]. Currently, bulk crystals of heavy LYSO:Ce and LGSO:Ce solid solutions are well-established scintillators for positron emission tomography (PET), with light yield (LY) of 30,000–35,000 photons/MeV [2, 4, 5]. Additionally, Lu_2SiO_5:Ce,Tb single crystalline films (SCFs), grown by the liquid phase epitaxy (LPE) method from PbO-B_2O_3 flux, are excellent candidates for scintillating screens in microimaging applications, offering submicrometric spatial resolution [6, 7].

Due to the high growth temperatures required for orthosilicate crystals, the complexity of their cation sublattices, and the presence of cations with the same charge state in different lattice sites, a variety of point defects can form. Of particular importance are vacancies and their complexes with other defects or impurities [3, 8]. For example, the well-known intense afterglow observed in Ce-doped orthosilicates is attributed to deep electron traps associated with oxygen vacancies [9, 10].

The concentration of such defects can be significantly reduced in scintillators grown at lower temperatures via LPE, producing SCFs from flux melts [11, 12]. However, the incorporation of flux components (mainly lead ions in the Pb^{2+} state) into the films may also influence their luminescent properties [12–14]. Therefore, a detailed comparison between the luminescent behaviour of oxide compounds in film and bulk crystal forms is essential to distinguish intrinsic luminescent characteristics from defect-related emissions. In this regard, the combination of conventional optical and luminescence methods with electron paramagnetic resonance (EPR) provides a robust approach to accurately interpret the luminescence mechanisms in these materials [3].

LSO and its lighter counterpart, Y_2SiO_5 (YSO), along with their solid solutions, crystallize in the monoclinic **C2/c** space group [15]. This structure contains two crystallographically distinct rare-earth (RE) sites: RE1 and RE2, with oxygen coordination numbers of 7 and 6, respectively (Fig. 1). Ce^{3+} ions, due to their larger ionic radius compared to Y^{3+} or Lu^{3+}, preferentially occupy the larger RE1 site (seven-fold coordination), as confirmed by optical studies [16] and EPR investigations on bulk crystals [17–20], because the larger ionic radius of Ce^{3+} is better accommodated by the higher coordination environment. In contrast, Ce^{4+} does not intrinsically favour the Lu1 site because of its smaller ionic radius and higher charge state. However, in the YSO:Ce and LSO:Ce SCFs grown by LPE method from a PbO-based flux, stabilization of Ce^{4+} at the Lu1 site is enabled by *extrinsic charge-compensation mechanisms*, primarily involving Pb^{2+} flux-related dopants and/or oxygen vacancies. The formation of Ce^{4+}–Pb^{2+} pair centers and Ce^{4+}–V_O-related defect complexes compensates the local charge imbalance and allows Ce^{4+} incorporation without structural rearrangement. Consequently, the actual Ce valence state at the Lu1 site is governed by the defect chemistry imposed by growth conditions and post-growth thermal treatment, rather than by an intrinsic site preference of the host lattice.

Our previous EPR measurements on bulk crystals [19, 20], along with other studies [17, 18, 21], have shown that Ce^{3+} ions in 7- and 6-fold coordination environments in orthosilicates produce clearly distinguishable EPR signals. Since the luminescence and scintillation properties of Ce-doped orthosilicates are strongly influenced by the site occupancy of Ce^{3+} ions [16], this aspect requires comprehensive investigation in SCFs as well. Our recent optical and EPR investigations of YSO:Ce and $(Y,La)_2SiO_5$:Ce SCFs, grown by LPE method [22], to confirm a such statemen.

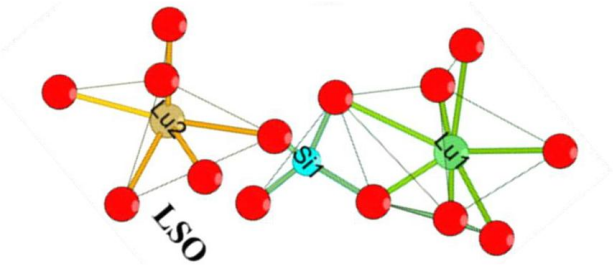


Fig. 1. Fragment of the Lu_2SiO_5 crystal structure showing the oxygen coordination environments (red circles) around the Lu1 and Lu2 sites.

Namely, the EPR measurements have revealed the presence of only one type of Ce^{3+} centers (Ce1) corresponding to the localization of the Ce^{3+} ions in the 7-fold coordinated Y positions of the Y_2SiO_5 host, and no Ce2 centers (Ce^{3+} ions in the 6-fold coordinated Y positions) were detected in these films.

However, detailed investigations of Ce^{3+} incorporation and its concentration dependence in LSO:Ce SCFs are lacking, and, to our knowledge, no EPR studies have been reported for these films. Meanwhile, given EPR's ability to resolve and quantify paramagnetic site occupancy, it represents an ideal tool for such an investigation and interpretation of basic phenomena of Ce^{3+} ions on LSO host.

The aim of the present study is to elucidate the peculiarities incorporation behaviour and site occupancy of Ce^{3+} ions in LSO:Ce SCFs grown by LPE method from conventional $PbO-B_2O_3$ flux, with particular attention to the dependence on Ce concentration. In addition, we investigate also the effects of thermal treatment (TT), considering variables such as temperature, duration, and atmosphere. Optimizing TT conditions is essential to enhance the scintillation performance of these materials. Our results demonstrate that TT serves as an effective means to modulate the valence state of Ce in LSO SCFs, thereby allowing fine-tuning of their luminescent and scintillation properties.

2. Peculiarities of the LPE growth of LSO:Ce SCF and their structural quality

Several sets of LSO:Ce SCFs were grown by the isothermal dipping LPE method onto 0.5 mm thick undoped YSO substrates with (001) and (110) orientations (Table 1). The growth was performed from a $PbO–B_2O_3$-based melt solution within a temperature range of 950–1005 °C. The SCFs were crystallized on both sides of the substrates with approximately equal thicknesses in the 5-25 μm range, as listed in Table 1. Two sets of YSO substrates were used: the (001)-oriented substrates were prepared from crystals grown from 5N high-purity starting materials, while the (110)-oriented substrates were obtained from crystals grown using 4N medium-purity material. In the latest substrates, trace impurities such as Gd^{3+}, Tb^{3+}, and Eu^{3+} were detected using luminescence and EPR spectroscopy.

Table 1. Growth conditions of Lu_2SiO_5:Ce SCFs, their light yield (LY) of radioluminescence (as grown and after TT in air (A) and N_2+H_2 (R) atmospheres) under excitation by α–particles of Pu^{239} (5.15 MeV) source measured with a shaping time of 12 μs in comparison with the standard YAG:Ce SCF sample with LY of 2650 Photon/MeV [24]. h is the SCF thickness, T_g and f_g are the SCF growth temperature and growth rate, respectively. * - SCF thickness is below passway of α–particles with energy of 5.15 MeV (around 10 μm) in LSO host. n. m. - not -measured; n. d. - not detected.

Number of SCF	Substrate	Total Ce content from MA, at. %	Ce^{3+} content from EPR: as grown/after TT in air (A) / in N_2+H_2, at. %	Pb content, at. %	h, μm	f_g, μm/min	T_g, °C	LY,% as grown	LY,% TT in air	LY,% TT in N_2+H_2
a1/a1-A/ a1-R	YSO(110)	1.07	0.15–0.3/ n. d. / 0.5–1	0.10	5	0.083	980	6*	n. d.	12*
a2	YSO(110)	1.28		0.13	35	1.02	970	4	n. d.	8
a3	YSO(001)	2.47		0.24	23	0.39	965	5	n. d.	9
a4	YSO(001)	2.59		0.34	>25	-	962	4	n. d.	10
b1/b1-R/ b1-A	YSO(001)	1.20	0.15–0.3 / n. d./ 0.5–1	0.12	9	0.05	970	7*	n. d.	14*
b2	YSO(110)				20	0.28	960	17	8	26
c1	YSO(110)	1.86		0.09	5	0.11	980	23*	15*	28*
c2	YSO(110)				9	0.13	975	15*	13*	19*

Cerium doping was introduced into the melt in the form of CeO_2 oxide at a concentration of 20 mol.%. Such a high concentration is required due to the very low segregation coefficient of cerium in orthosilicate SCFs, which is only 0.003–0.005 during the crystallization of LSO SCFs on YSO substrates [22, 23]. Although the lattice misfit between the film and substrate is non-negligible, partial compensation occurs due to the incorporation of larger cerium and lead ions in place of lutetium cations. The detailed growth conditions for the LSO:Ce SCFs are presented in Table 1 and have been previously described in our earlier publications [22, 23].

We have found, that the morphology of the crystallographic planes of LSO and YSO attics is very important factors which determined occurrence of stable LPE growth of high-quality LSO based films onto YSO substrates. The Fig. 2 present the views of the fragments of the YSO and LSO elementary cells [24, 25]. As can see from these figures, the crystallographic planes corresponding to the (001) and (110) for of YSO as well as (110) and (101) for LSO, respectively, are fully overlapped. That means, the crystallization of the LSO:Ce SCFs with (010) and (101) plane orientations will be occurs onto YSO substrates with (001) and (110) orientations, respectively.

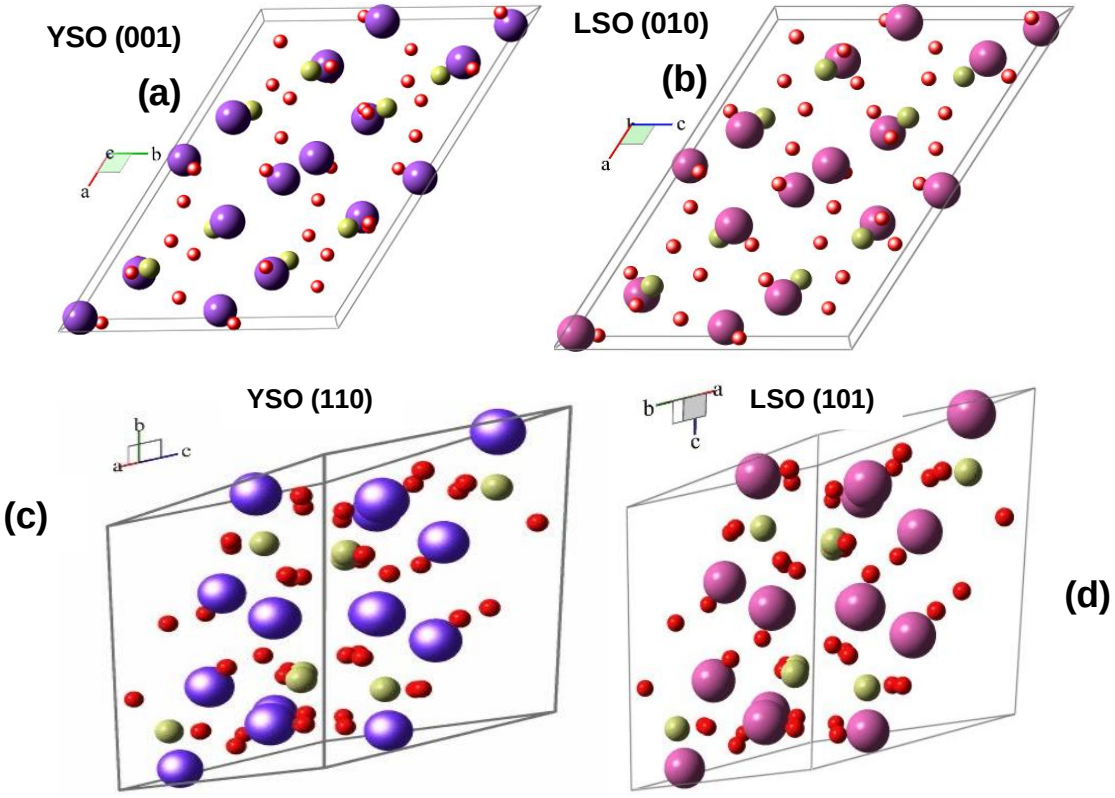


Fig. 2. Crystal structures of YSO (a, c) and LSO (b, d) elementary cells. The screen plane corresponds to the (001) (a) and (010) (b) planes, and the (110) (c) and (101) (d) planes for YSO and LSO hosts, respectively [24, 25].

To characterize the quality of the SCFs, we employed both visual surface inspection using a Keyence digital optical microscope at 100× magnification and X-ray diffraction (XRD) analysis using a modified DRON-4 double-crystal diffractometer (Fig. 3). The XRD results fully confirm the previously mentioned conclusions regarding the crystallographic orientation of the LSO:Ce SCFs relative to the YSO substrate planes. Our findings indicate that the (010) plane is the preferred orientation for LSO:Ce SCF crystallization onto (110) oriented YSO substrates (Table 1 and Fig. 3a). Notably, these SCFs exhibited superior structural quality, even at relatively high growth rates ranging

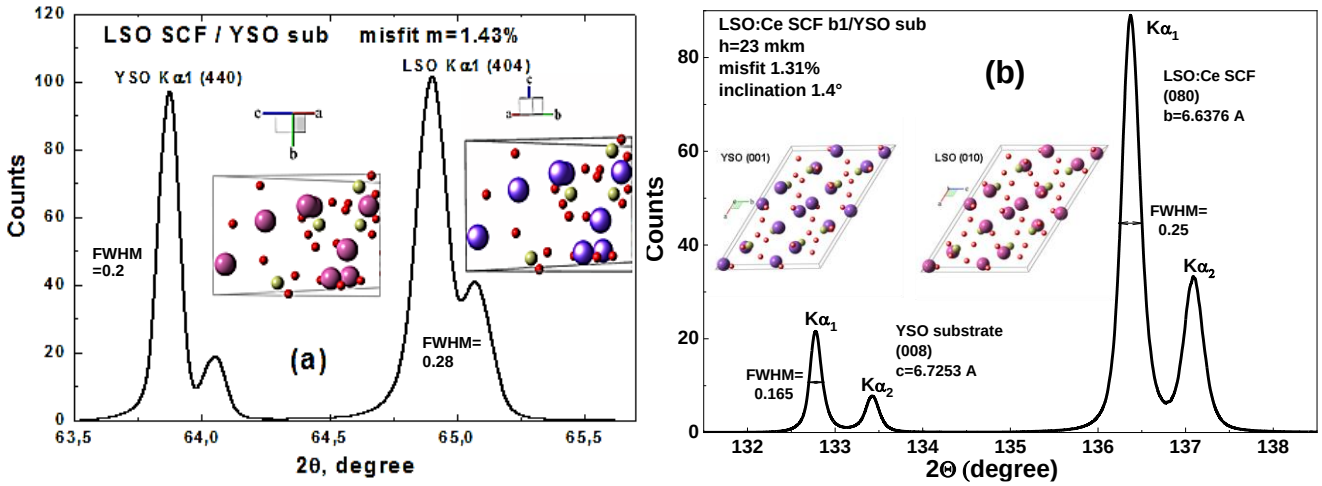


Fig. 3. Double-crystal XRD patterns of the (404) and (080) reflections of LSO:Ce a1 and b1 SCFs grown on YSO substrates with (110) (a) and (001) (b) orientations, respectively. The Miller indices of the observed reflections are indicated. *Inset:* Fragmented lattice schematics of YSO (left) and LSO (right), demonstrating the good structural matching of the corresponding planes. The front plane in each schematic corresponds to the (101) and (010) planes of LSO in (a) and (b), respectively, and to the (110) and (001) planes of YSO in (a) and (b), respectively.

from 0.08 to 1 μm/min. For example, the full width at half maximum (FWHM) values of the diffraction peaks for the (101) oriented LSO:Ce a1 SCF sample are equal to 0.28 degree in comparison with 0.2 degree of the YSO (110) crystal substrate (Fig. 3a), indicating excellent structural perfection of films. These results demonstrate that the use of (110) oriented YSO substrates significantly enhances the crystalline quality of LSO:Ce SCFs.

However, the structural quality of LuAG:Ce SCFs with (010) orientation grown on (001)-oriented YSO substrates was notably worse than that of films grown on substrates with (110) orientation. This effect appears to be largely independent of the SCF/substrate lattice misfit, which is 1.43% for the LSO:Ce SCF (101)/YSO(001) substrate structure (Fig. 2a) and 1.31% for the LSO:Ce SCF (010)/YSO (001) substrate structure (Fig. 2b). Interestingly, the FWHM values of the diffraction peaks for the (010) oriented LSO:Ce b1 SCF are only slightly larger (0.25°) than those of the YSO (001) crystal substrate (0.165°) (Fig. 3a), indicating very good structural perfection of the film.

To investigate this phenomenon in more detail, we measured the rocking curves of (060) reflection peak in LSO:Ce SCF (010)/YSO(001) substrate structure using a double-crystal X-ray diffractometer in both 2θ and 2ω modes (Figs. 4a and 4b). These measurements allow us to estimate lattice distortion due to strain, expressed as Δa/a. The resulting rocking curves, presented on the same scale in Fig. 4b, show that the observed broadening is primarily due to lattice deformation rather than a change in lattice parameter. This suggests that the quate poorer structural quality in the (001)-oriented SCFs is likely caused by significant deformation due to the larger effective mismatch between the LSO:Ce SCF (010)/YSO(001) substrate interface, even though the nominal lattice misfit is slightly smaller.

The composition of SCF samples was determined using a JEOL JSM-820 electronic microscope, equipped by EDX microanalyzer (MA) with IXRF 500 and LN2 Eumex detectors. The sample content was determined in five points with the accuracy within 100 ppm (0.01 at. %) and the results were averaged. It is important to note that the growth temperature has strong influence on the Ce and Pb concentration in SCFs. Generally, the content of Ce and Pb ions increases with decreasing temperature of SCF crystallization and vice versa (Table 1). For instance, the Ce

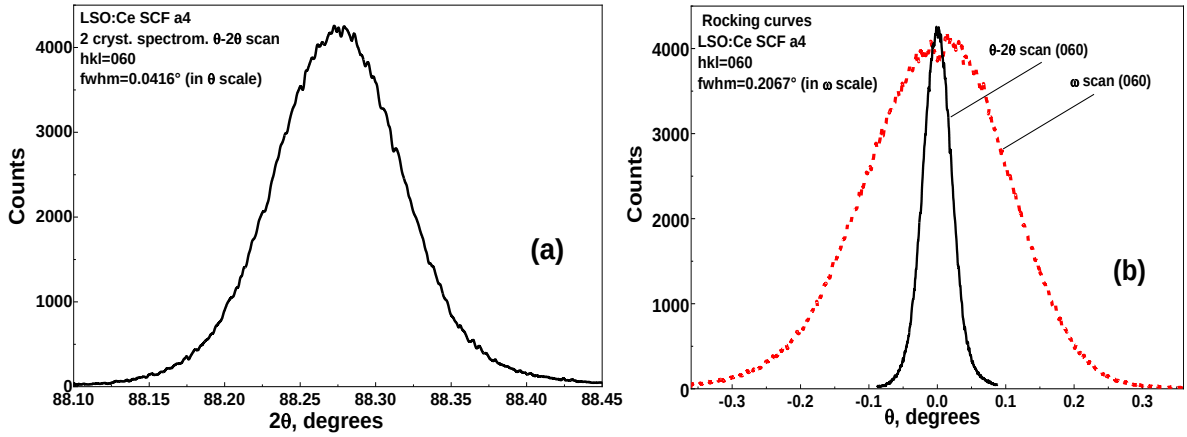


Fig. 4. Fragment of double-crystal XRD patterns of the (060) reflections of LSO:Ce SCF a4 (a) and rocking curves of the (060) reflection in this sample, recorded in 2θ and ω modes (b).

concentration is 1.07 at.% in the LSO:Ce a1 SCF grown at 980 °C, and it notably increases to 1.28 at.% when the growth temperature of the LuAG:Ce a2 SCF decreases to 970 °C. The highest Ce concentrations, 2.47 and 2.59 at.%, are observed in the Lu_2SiO_5:Ce a3 and a4 samples, grown at 965 °C and 962 °C, respectively. From the analysis of the content of LSO:Ce SCFs (Table 1), we found also that the cerium segregation coefficients in LSO host at LPE growth of these SCFs, grown onto YSO substrates, are significantly influenced by growth temperature and are equal to 0.054 for LSO:Ce a1 SCFs and significantly increase to 0.13 in LSO:Ce a4 SCF.

3. Experimental technique for optical and EPR studies

For characterization of the optical properties of LSO:Ce SCFs after LPE growth and TT in air (A) and reduction (R) (95 % H_2+ 5% N_2) atmospheres the absorption spectra, cathodoluminescence (CL) spectra, pulse height spectra (PHS), light yield (LY) and scintillation decay kinetics under excitation by α–particles of ^{239}Pu (5.15 MeV) were measured for all sets of samples presented in Table 1. The absorption spectra were recorded using a Jasco V730 spectrophotometer within the 200 to 1100 nm wavelength range. The cathodoluminescence (CL) spectra were measured with using a JEOL JSM-6390LV scanning electron microscope (SEM) as e-beam source with an electron beam energy of 20 kV. This SEM was equipped also with a Stellar Net spectrometer, completed with a cooled TE-detector CCD, functioning within the 200-1200 nm range. The measurements of scintillation pulse height spectra (for LY determination) and decay kinetics of the SCF scintillators were performed using a setup consisting of a Hamamatsu H6521 photomultiplier, a multichannel analyzer, a Tektronix TDS3052 digital oscilloscope. The selected YAG:Ce SCF sample used as a reference, with a light yield (LY) of 2650 photons/MeV.

Ce^{3+} EPR spectra were acquired with a Bruker X-/Q-band E580 FT/CW ELEXSYS spectrometer at X- band with the microwave frequency 9.4 GHz at the temperature of 4–20 K. For the EPR investigations we have selected two LSO:Ce a1 and b1 SCFs, catted for 3 peace's. The first peace was annealed at 1100^{o}C during 7 hours in reduction N_2+H_2 atmosphere (a1-A, b1-R) while second peace was annealed in air at 1250 ^{0}C during 4 hours (a1-A, b1-A). The third peace of LSO:Ce SCF a1 was used as the reference sample. From the EPR measurements, approximate Ce^{3+} concentration was determined and its dependence on annealing atmosphere of films (see Table 1).

4. Experimental results and discussion

4.1 Absorption spectra of LSO:Ce SCF

The absorption spectra of several as-grown LSO:Ce SCFs, produced from PbO-based fluxes, are shown in Fig. 5a, in comparison with the absorption spectra of the respective YSO substrate. In contrast to the YSO substrate, in which no absorption was detected in the spectral range above 210 nm, the absorption spectra of the LSO-based SCFs grown from PbO-based fluxes exhibit characteristic intensive bands in the UV range, peaking at 210, 232, and 257 nm. The intensity of these bands increases with increasing SCF thickness and decreasing SCF growth temperature; i.e., with increasing Pb^{2+} content in the SCFs and vice versa [26, 27] (Fig. 5a). Therefore, these bands are attributed to absorption by Pb^{2+} flux-related impurities. Specifically, the bands peaking at 257, 232, and 210 nm correspond to the $^1S_0 \rightarrow {}^3P_1$, $^3P_2$, and $^1P_1$ transitions of Pb^{2+} ions (A, B, and C bands), respectively[9]. These bands may also overlap with broad bands in the same spectral range related to charge transfer transitions (CTT) between Pb^{2+} ions and the bottom of the LSO conduction band [26, 27].

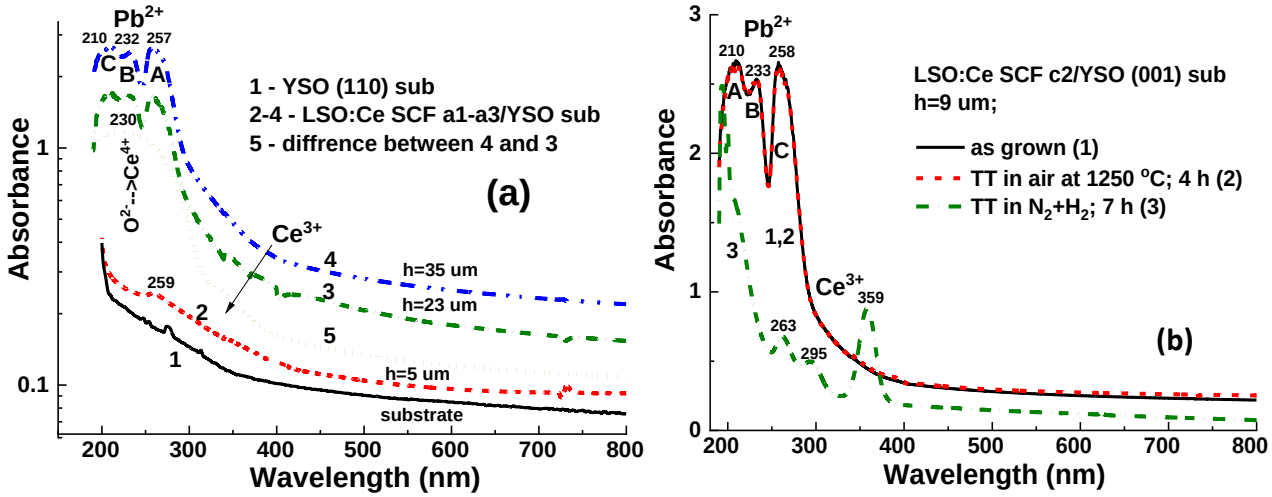


Fig. 5 (a) - absorption spectra (logarithmic scale) of LSO:Ce SCFs with various thicknesses and grown at different temperatures (a1-a3 samples; see Table 1), compared with the absorption spectrum of the YSO substrate. Curve 5 shows the difference between spectra 4 and 3. (b) - evolution of the absorption spectra of LSO:Ce c2 SCF at 300 K: as-grown (curve 1), after thermal treatment (TT) in air (curve 2), and after reduction in $N_2 + H_2$ atmosphere (curve 3). T=300 K.

It should also be mentioned that due to the high concentration of lead ions in the SCFs grown from PbO-based fluxes, the formation of Pb^{2+}–V_O–Pb^{2+} dipole centers is expected, where V_O represents oxygen vacancies, providing local charge and volume compensation. Another possible mechanism for such charge and volume compensation is the formation of Pb^{2+}–Pb^{4+} pairs at high lead concentrations in the SCF samples [9, 10]. For this reason, it is also possible that the weak, continuous absorption of LSO:Ce SCFs across the entire spectrum up to 800 nm (Fig. 5a) is partially caused by $Pb^{2+} \rightarrow Pb^{4+}$ CTT [28].

In principle, the small bump observed around 360 nm in the spectra of LSO:Ce SCFs grown from PbO flux can be attributed to the 4f–5d$_1$ transitions of Ce^{3+} ions in the LSO host. However, the concentration of Ce^{3+} ions in the as-grown LSO:Ce SCFs is very low, as the main Ce^{3+} absorption band at 360 nm appears only as a slight bump on the low-energy wings of the strong absorption bands associated with intrinsic transitions of Pb^{2+} ions.

Therefore, the dominant valence state of cerium ions in these as-grown SCFs *is not* Ce^{3+}. Considering the very high concentrations of lead in the LSO:Ce SCF samples (0.1–0.34 at.%, see Table 1), we may infer the formation of Ce^{4+}–Pb^{2+} pair centers in these SCFs, providing local charge and volume compensation.

This conclusion is further supported by the presence of strong, broad bands in the 200–350 nm range, peaking around 230 nm, in the differential absorption spectra of LSO:Ce SCFs of varying thickness (Fig. 5a, curves 2–4). This band in the absorption spectra of the mentioned SCF samples may correspond to $O^{2-} \rightarrow Ce^{4+}$ CTT, due to the formation of Ce^{4+}–Pb^{2+} pair centers in the LSO:Ce SCFs grown from PbO-based flux 26, 27.

The TT in air at 1250 °C (more than 250 °C higher than the growth temperature) does not significantly alter the structure of the absorption bands of LSO:Ce SCF (Fig. 5b, curve 2). Only a slight overall increase in UV absorption intensity was observed, without any significant change in the intensity of the bands at 257, 232, and 210 nm, which correspond to the $^1S_0 \rightarrow {}^3P_1$, $^3P_2$ and $^1P_1$ transitions transitions of Pb^{2+} ions, respectively.

Considering the formation of Ce^{4+}–Pb^{2+} pair centers, this suggests that the Ce^{3+} concentration in the SCFs annealed in air decreases compared to the as-grown samples, due to the formation of additional pair centers, in accordance with the following reaction:

$$\mathbf{2Ce^{3+} + (Pb^{2+} - V_O - Pb^{2+}) \text{ pairs} \rightarrow TT \text{ in air} \rightarrow 2(Ce^{4+}\text{-}Pb^{2+}) \text{ pairs} + O^{2-}} \quad (1)$$

where V_O denotes an oxygen vacancy. It is also possible that a part of the Pb^{2+} ions oxidize to the Pb^{4+} state, leading to the formation of Pb^{2+}–Pb^{4+} pair centers. Such centers may be responsible for the slight increase in visible-range absorption observed in LSO:Ce SCF treated in air, due to $Pb^{2+} \rightarrow Pb^{4+}$ CCT (Fig. 5b, curve 2).

In contrast, TT in a reducing atmosphere of $N_2 + H_2$ causes significant changes in the absorption spectra of LSO:Ce SCFs grown from a PbO flux (Fig. 4b, curve 3). Specifically, Ce^{3+} ions in the annealed SCFs were revealed through the appearance of additional absorption bands in the UV region, peaking at 263, 295, and 359 nm. These bands correspond to the Ce^{3+} 4f–5d transitions in the LSO host (Fig. 5a, curves 3 and 4). The first Ce^{3+}-related absorption band at 263 nm overlap with the Pb^{2+} absorption bands in this spectral range. This suggests that some Ce^{4+} ions were reduced back to Ce^{3+} due to the formation of oxygen vacancies, in accordance with the reaction:

$$\mathbf{2(Ce^{4+}\text{-}Pb^{2+}) \text{ pairs} \rightarrow TT \text{ in } N_2 + H_2 \rightarrow 2Ce^{3+} + V_O + 2Pb^{2+}} \quad (2).$$

4.2 CL spectra of LSO:Ce SCFs

The CL spectra of as-grown LSO:Ce SCFs, prepared using a PbO-based flux, are primarily composed of a superposition of the following components: (i) UV emission bands peaking at 337–340 nm, originating from the flux-related Pb^{2+} impurity and corresponding to the $^3P_{1,0} \rightarrow {}^1S_0$ intrinsic transitions of Pb^{2+} ions located at Lu1 sites in the LSO host, where they are seven-fold coordinated by oxygen ions (Pb1 centers); (ii) visible emission bands peaking at 441–445 nm, attributed to the luminescence of excitons localized around Pb^{2+} centers; and (iii) a broad emission band peaking at 492 nm, associated with luminescence from dimer Pb^{2+}–Pb^{2+} centers (Fig. 6a) [26, 27, 29].

Due to the low Ce^{3+} concentration in the as-grown SCF samples, Ce^{3+} luminescence appears only as a weak bump around 410 nm, which overlaps with the emission from excitons localized around Pb^{2+} centers. In addition to emissions from Pb^{2+} and Ce^{3+} centers, strong luminescence bands from trace impurities of Eu^{3+} and Tb^{3+} are also observed in the CL spectra of as-grown LSO:Ce SCFs, appearing in the orange-red and green spectral regions, respectively.

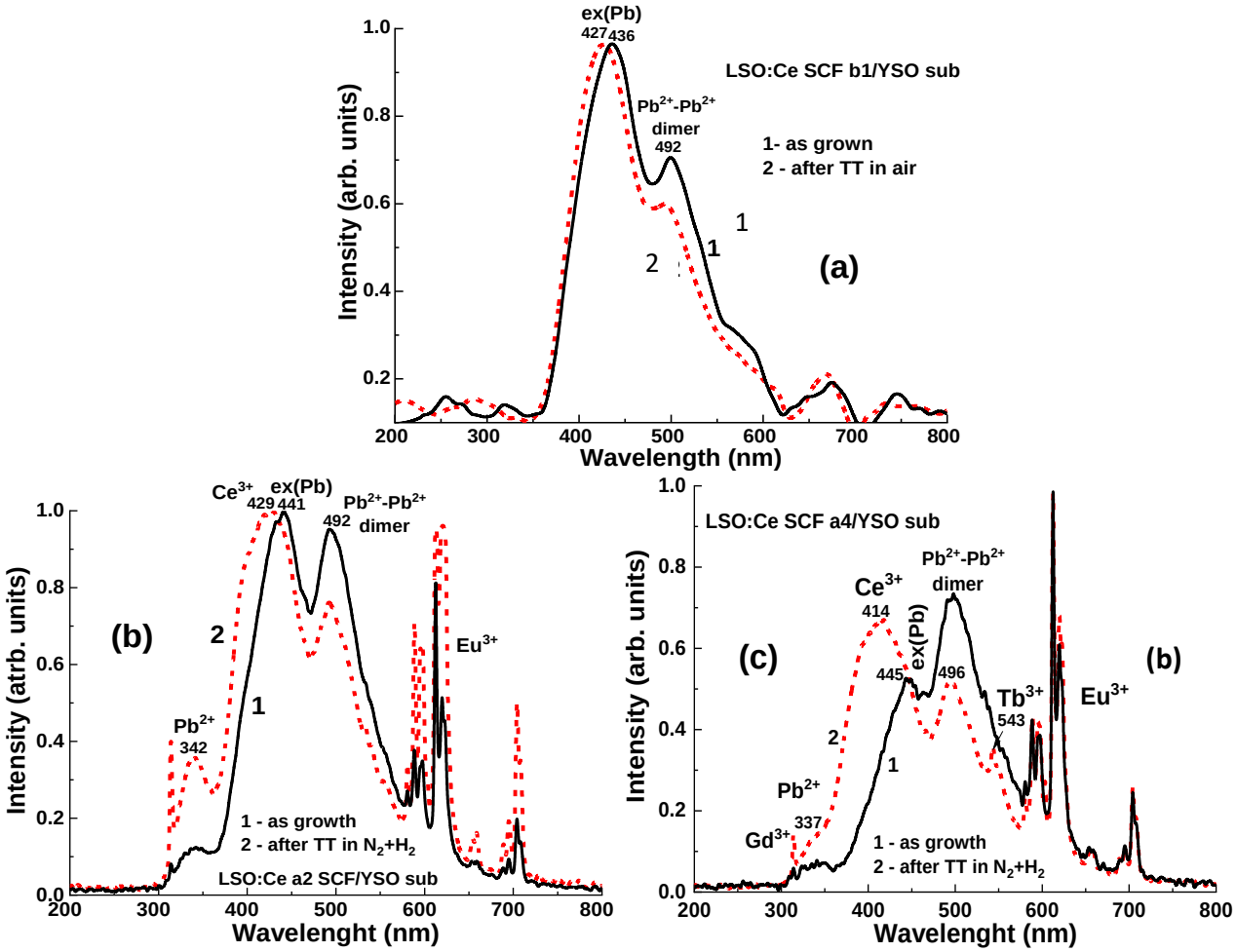


Fig.6 (a) - RT CL spectra of LSO:Ce b1 SCF samples: as-grown (curve 1) and after thermal treatment (TT) in air at 1250 °C (curve 2). (b, c) - RT CL spectra of LSO:Ce a2 and a4 SCFs samples: as-grown (curves 1) and after TT in a reducing $N_2 + H_2$ atmosphere (curves 2).

TT of the LuAG:Ce SCF sample in an air results in a notable decrease in the intensity of the Pb^{2+}–Pb^{2+} dimer emission band at 492 nm and a complete elimination of the intrinsic luminescence of isolated Pb^{2+} centers in the 340 nm band, in accordance with reaction (1) (Fig. 6a, curve 2). This treatment also causes a slight blue shift of the exciton-related Pb emission band (ex(Pb) center) from 436 nm to 427 nm.

Meanwhile, the CL spectra of LSO:Ce SCFs a2 and a4 annealed in a reducing $N_2 + H_2$ atmosphere exhibit broad, complex emission bands peaking at 414–429 nm (Fig. 4a and 4c). These are attributed to the $5d_1$-4f ($^2F_{5/2,7/2}$) radiative transitions of Ce^{3+} ions occupying Lu1 sites in the LSO host, where they are coordinated by seven oxygen atoms (Ce1 centers) [11-13, 29]. The appearance of the Ce^{3+} emission band is also accompanied by an increase in the luminescence of isolated Pb^{2+} ions in the 342 nm band and a corresponding decrease in the intensity of the Pb^{2+}–Pb^{2+} dimer centers at 492 nm (Figs. 6b and 6c). These results further confirm the Ce^{4+}–Pb^{2+}→Ce^{3+} + Pb^{2+} transformation in LSO:Ce SCFs after reduction treatment, in accordance with reaction (2).

4.3 Scintillation properties of LSO:Ce SCFs

We have found that lead contamination has a strongly negative impact on the scintillation properties of LSO:Ce SCFs. All LSO:Ce SCF samples listed in Table 1, grown using a PbO-based flux, exhibit low LY in the range of 4–

23%, compared to the reference YAG:Ce SCF sample with LY of 2650 photons/MeV (100%) under α-particles excitation from a ^{239}Pu (5.15 MeV) source. This reduced LY is primarily due to the low segregation coefficient of Ce^{3+} ions in the LSO host during LPE growth, resulting in relatively low Ce concentrations in the films. Additionally, a significant amount of Pb^{2+} contamination from the flux strongly quenches Ce^{3+} luminescence [27, 29, 30].

The combination of high Pb contamination ranging from 0.1 to 0.34 at. % and the low Ce^{3+} segregation coefficient (0.054–0.12) are the main reasons for the significantly lower LY of Ce-doped LSO SCFs compared to their single-crystal counterparts [27, 29, 30]. In these as-grown SCFs, which have a high cerium content but a low concentration of Ce^{3+} ions, the Ce^{3+}/Pb^{2+} ion ratio does not exceed 1.5–3 (Table 1), which is significantly lower than the typical ratio (15–16) observed in YAG:Ce and LuAG:Ce [31, 32]. As a result, even the best-performing LSO:Ce SCF samples exhibit LY values that are 4–7 times lower than those of high-quality LYSO:Ce bulk crystals [27, 29, 30], see also Table 1. This degradation can be attributed to: (i) the high concentration of lead ions in the SCFs, and (ii) the likely preferential formation of less-effective luminescent Ce^{4+}–Pb^{2+} complexes instead of high-effective luminescent Ce^{3+} centers.

Changes in the Ce ion valence state induced by TT significantly affect also the LY, decay time, and afterglow behaviour of LSO:Ce scintillators. We also found that the LY of LSO:Ce SCFs under α-particles excitation decreases after annealing in an air atmosphere, becoming even lower than in the as-grown samples (Table 1). This reduction is attributed to the near-complete recharging of Ce^{3+} ions into the Ce^{4+} state. Since the scintillation efficiency of Ce^{3+} centers is significantly higher than that of Ce^{4+}–Pb^{2+} complexes [27, 29, 30], the LY of the SCFs declines following thermal treatment (TT) in air. In contrast, annealing in a reducing $N_2 + H_2$ atmosphere results in a notable increase in the LY of SCF samples, due to the formation of a high concentration of Ce^{3+} centers.

Interestingly, TT in an air atmosphere markedly accelerates the scintillation decay kinetics of LSO:Ce SCFs compared to the as-grown samples. This is attributed to the formation of Ce^{4+} centers and a reduced influence of oxygen vacancies on the scintillation process (Fig. 7, curve 2). It is well known that doping LSO:Ce scintillators with divalent ions such as Ca^{2+}, Mg^{2+}, or Pb^{2+} leads to a decrease in light yield and a shortening of the scintillation decay time [27, 33, 34]. This effect is consistent with more efficient electron trapping by Ce^{4+} ions compared to Ce^{3+} centers. In the latter case, Ce^{3+} ions initially trap holes, which delays energy transfer to the emission centers and

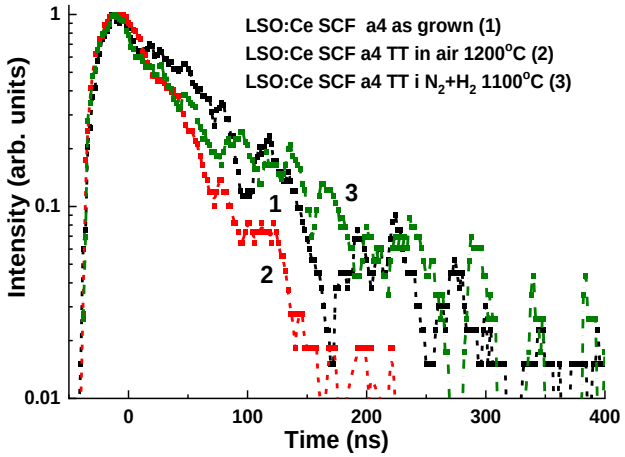


Fig. 7. Scintillation decay kinetics of LSO:Ce SCFs a4 under particles excitation by ^{239}Pu (5.15 MeV) source: as grown samples (1) and after TT in air at 1250°C (2) and N_2+H_2 atmosphere at 1100°C (3).

results in slower scintillation decay. In contrast, TT in a reducing N_2 + H_2 atmosphere promotes the formation of oxygen vacancies, which act as efficient electron traps. This increases the energy migration time from the host lattice to Ce^{3+} centers, resulting in slower scintillation decay kinetics (Fig. 7, curve 3).

It should be noted that the oxygen vacancy concentration in the as-grown and thermally treated samples is not directly measured in the present work, e.g., by positron annihilation spectroscopy or thermoluminescence. Instead, our discussion of the role of oxygen vacancies in scintillation decay kinetics is based on indirect but well-established experimental correlations between the thermal treatment atmosphere, Ce^{3+}/Ce^{4+} valence state conversion, and scintillation response in Ce-doped orthosilicates. In particular, the following experimental observations support our interpretation.

(i) EPR measurements (Part 4.4) clearly demonstrate a reversible conversion between Ce^{3+} and Ce^{4+} upon annealing in reducing (N_2+H_2) and oxidizing (air) atmospheres, respectively. Since Ce^{4+} is charge-compensated predominantly by oxygen vacancies in oxide hosts, the observed valence changes imply corresponding variations in oxygen vacancy concentration.

(ii) Systematic changes in scintillation decay kinetics are consistently correlated with annealing atmosphere: faster decay after air annealing and slower decay after reduction TT. This behavior is in line with the widely accepted role of oxygen vacancies as electron traps that prolong carrier migration and scintillation decay in LSO-based scintillators. The proposed mechanism is fully consistent with earlier studies on LSO:Ce and related orthosilicates, where oxygen vacancies were identified as dominant deep trapping centers affecting decay kinetics and afterglow (Refs. [3, 9, 10, 27]).

4.4. EPR of LSO:Ce SCF/YSO epitaxial structures after TT in air and reducing atmosphere

The incorporation of Ce^{3+} into LSO films was further investigated through EPR measurements. Both YSO and LSO hosts belong to the monoclinic C2/c symmetry group [15]. The lattice structure accommodates two distinct yttrium or lutetium sites Y1/Lu1 and Y2/Lu2, which are surrounded by seven and six oxygen neighbors, respectively. According to previous published data, Ce^{3+} ions preferentially occupy the Y1/Lu1 positions (Ce1 centers, about 95% in bulk crystals) [16, 17]. Moreover, each of these sites provides two magnetically inequivalent positions for the impurity ion. As a result, EPR spectra of a paramagnetic particle located at a regular yttrium or lutetium site will exhibit a characteristic doubling of the resonance lines [18, 19, 20]. Since Ce^{3+} has only one electron on its outer shall (electron configuration $4f^1$), the electron spin of this ions is S = 1/2 and thus only two spectral lines are expected for Ce^{3+} in the LSO lattice.

The EPR spectra were measured on three samples cut from the LSO:Ce SCF a1. This film was grown on a high quality undoped YSO substrate with a crystallographic orientation of (110) (Table 1) and a negligibly small concentration of incident paramagnetic impurities, which could otherwise mask the relatively weak signal from the film. The following samples were prepared: a1– as-grow; a1-A – annealed in air at 1250^0C during 4 h and a1-R– annealed in reduction N_2+H_2 atmosphere at 1100^0C during 7h. Additional measurements were performed on sample LSO:Ce SCF b1 annealed in N_2+H_2 atmosphere (sample b1-R), where the Ce^{3+} EPR spectrum was observed from the film. The samples were mounted on the holder such that the static magnetic field **B** was rotated within the plane of the films, specifically in the (110) plane. Temperature-dependent measurements (Fig. 8) allowed us to identify

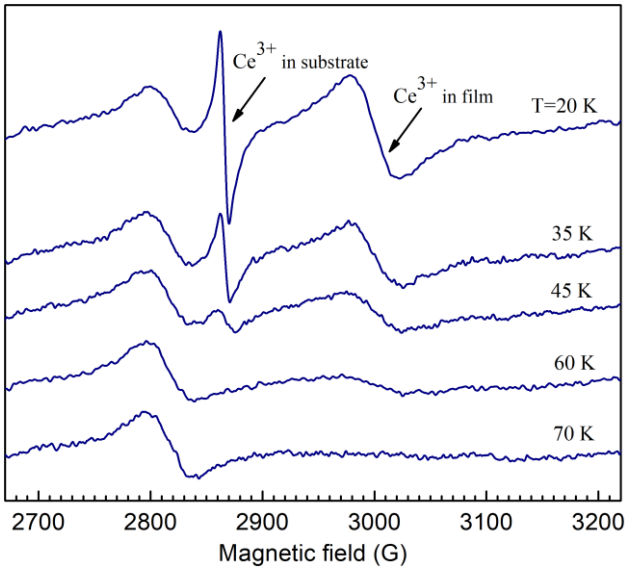


Fig. 8. EPR spectra of the LSO:Ce SCF a1-R /YSO (110) substrate sample at temperatures between 20 and 70 K, with the magnetic field applied parallel to the c-axis, showing the appearance of the Ce^{3+} signal in both the LSO film and the YSO substrate below approximately 60 K.

the signals from the paramagnetic Ce^{3+} ions, as the Ce^{3+} spectral lines were clearly visible only below ~50 K. At higher temperatures, the Ce^{3+} spectral lines broadened exponentially with temperature due to an increased spin-lattice relaxation rate and eventually become completely invisible.

The LSO:Ce SCF/YSO substrate samples exhibited Ce^{3+} spectral lines even from substrate. The Ce^{3+} lines were attributed to the films and to the substrates by using characteristic g-factor values at B || c for bulk LSO:Ce and YSO:Ce [18, 19]. Additionally, the spectral line from the YSO substrate was much narrower compared to that from the film (peak-to-peak linewidth of 7.8 G and 36-40 G, respectively), due to very small concentration of Ce ions in the substrate. In the films, the much higher Ce^{3+} ion concentration (~ 0.5-1 at.%) leads to significant broadened of the spectral lines due to magnetic dipole interactions between Ce^{3+} spins. It should also be noted that the Ce^{3+} signal in the LSO:Ce SCF disappears at higher temperatures relative to that in the YSO substrate, which is consistent with the fact that spin-lattice relaxation is faster in YSO [18].

Since the LSO:Ce films were grown on a substrate cut in the (110) plane, this plane does not contain any of the principal directions of the g tensor. However, it contains the [001] (c-axis) crystallographic direction, which is close to the principal direction of the largest g-tensor component, g_3 = 2.348 for YSO and 2.250 and LSO [18, 19]. The angular dependence of the resonance field around the c direction is also relatively flat [18, 19]. Thus, the resonance field does not change markedly when the magnetic field deviates from the g tensor principal direction and reaches a minimum when aligned along the c-axis. This is illustrated in Fig. 9, which shows the angular dependence of resonance fields measured for Ce^{3+} in the LSO:Ce SCF and YSO substrate. Specifically, the angular dependence was used to orient the samples within the spectrometer cavity to find the direction along the c-axis. Sample LSO:Ce SCF a1-R was oriented only approximately due to the absence of a distinct Ce^{3+} EPR signal. Therefore, a background EPR spectrum from an unknown impurity was used to orient this sample with respect to the crystallographic axes.

The angular dependencies presented in Fig. 9 were fitted using the g tensor parameters from literature data

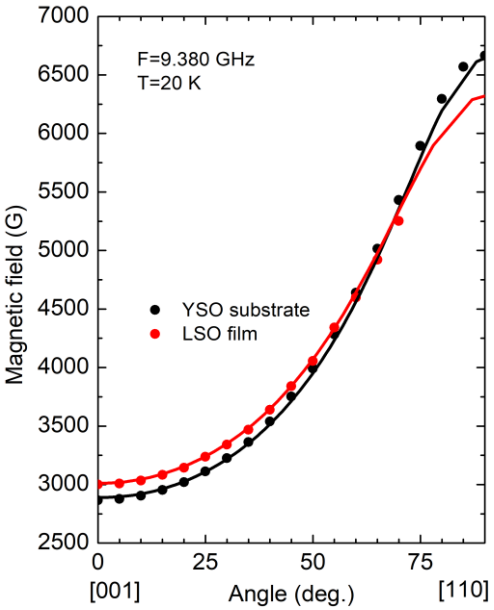


Fig. 9. Angular dependence of Ce^{3+} resonance fields in the YSO substrate (black points) and in the LSO:Ce SCF a-R (red points) as the magnetic field is rotated in the (110) plane. Solid lines represent the calculated resonance fields using spin Hamiltonian parameters taken from Ref. [19].

for Ce^{3+} at the Y1/Lu1 positions of YSO and LSO crystals [18, 19]. A good agreement is observed between the measured (points) and calculated (solid lines) resonance fields. Since the resonance fields in YSO and LSO at B || c differ significantly from each other, the EPR signals from the film and substrate are clearly distinguishable. We also looked for the EPR signal from Ce^{3+} at the second Y2/Lu2 positions (Ce2 centers). Their resonance fields at B || c are expected to be at magnetic field around 7000 G. Fig. 10 shows EPR spectra measured for two samples, #a-R and #b-R, at fields up to 8000 G. Weak EPR signals from two magnetically non-equivalent Ce2 centers are

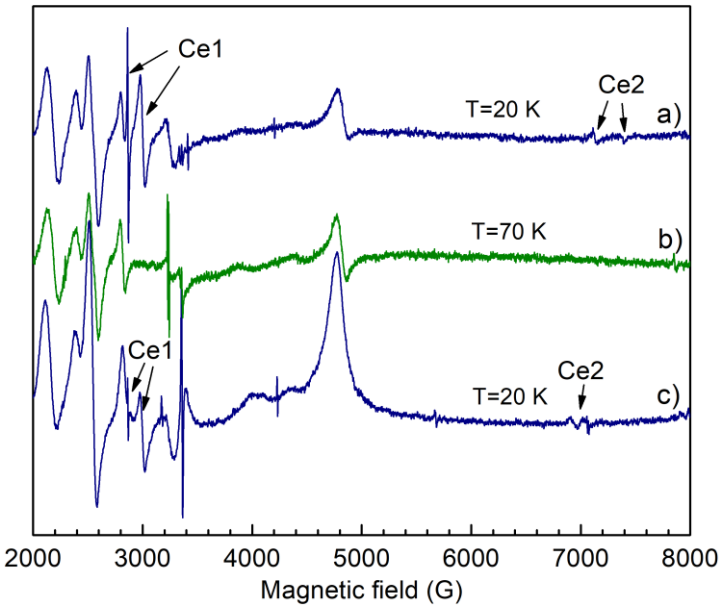


Fig. 10. EPR spectra measured in LSO:Ce SCFs/YSO substates structures at B || c and T = 20 and 70 K. (a) EPR spectrum of a1-1 sample at 20 K, (b) at 70 K, and (c) EPR spectrum of b1-R sample at 20 K. EPR signals from both Ce1 and Ce2 centers are observed only in the YSO substrate.

clearly observed at the expected field around 7000 G. The Ce2 signal does not visible at 70 K, similar to Ce1 signal. The linewidth of the Ce2 spectral lines is ≈20 G, suggesting that the Ce2 centers belong to the substrate. In the case of the film, the linewidth should be much broader due to the high total concentration of Ce^{3+} ions. At least, it should not be narrower than the linewidth of the Ce1 centers. A similar Ce2 spectrum is observed in another b1-R SCF sample, which was grown on a substrate from the same YSO crystal. Consequently, no Ce2 centers were detected in EPR spectra from the films, indicating that their fractional content Ce2/(Ce1+Ce2) in the films is much smaller than in the substrate.

Fig. 11 shows the spectra fragments containing the Ce^{3+} EPR signals at B || c and T = 20 K for all three LSO:Ce SCF a1 samples (a1, a1-A and a1-R). Compared to the as-grown sample, the sample annealed in air shows no detectable signal from Ce^{3+} in either the film or substrate, indicating that the thermal treatment in air reduces the concentration of paramagnetic Ce^{3+} centers both in film and substrate. In contrast, annealing in an N_2+H_2 atmosphere significantly increases the Ce^{3+} content by approximately 3 times in the film and 5 times in the substrate. Thus, thermal treatment significantly influences the Ce valence state in both YSO and LSO orthosilicates. This confirms that annealing in oxygen-rich atmospheres (air) reduces oxygen vacancies, leading to the conversion of Ce^{3+} to non-paramagnetic Ce^{4+}. Conversely, annealing in a reducing atmosphere promotes the reduction of non-paramagnetic Ce^{4+} to paramagnetic Ce^{3+} ions by creating oxygen vacancies.

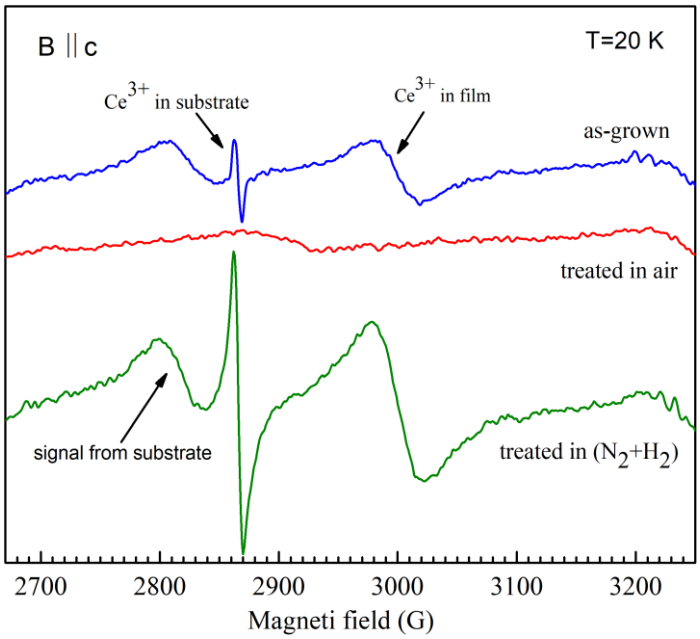


Fig.11. EPR spectra measured in the LSO a1 SCF at B || c and T=20 K for three samples: as-grown, annealed in air, and annealed in an N_2+H_2 atmosphere. The spectra are normalized in intensity to the same sample volume.

Finally, let us estimate the concentration of Ce^{3+} ions in the LSO SCFs where the EPR signal was observed. This can be done using the dipole-dipole broadening of the Ce^{3+} spectral lines. The dipole broadening can be usually expressed through the second moment of the EPR line as [35]:

$$M_2 \approx 5.1(g\beta N)^2 S(S+1),$$

where N is the number of spins per cubic centimetre, S = 1/2 and g = 2.234 are the Ce^{3+} spin and g factor at B || c, respectively, and β is the Bohr magneton. Dipole broadening results in a Gaussian line shape. In this case, the

second moment can be determined directly from the half-intensity linewidth as $W_G = \sqrt{M_2}$. In the measured films, however, the line shape is not pure Gaussian, indicating that imperfections contribute to the linewidth. Consequently, the second moment and therefore the spin concentration estimated from the linewidth may be overestimated by up to a factor of two. Considering this, the Ce^{3+} concentration calculated from the EPR spectra is in the range of 0.15–0.3 at.% for the as grown a1 and b1 films and increases to approximately 0.5–1 at.% in the a1-R and b1-R films annealed in an H_2+N_2 atmosphere. Despite the relatively large error margin, this method offers advantages over the conventional spin-counting approach based on double integration of the EPR spectrum and comparison with a reference sample. This is particularly relevant when the EPR signal is weak. For example, double integration introduces significant error due to contributions from the substrate and other background signals, which are comparable in intensity to the Ce^{3+} signals in films. In addition, saturation effects at low temperatures in reference sample (commonly MgO:Mn or MgO:Cr) further increase the uncertainty to the calculation.

5. Discussion

As noted in Section 4.4, the Lu_2SiO_5 host lattice contains two crystallographically distinct lutetium sites, Lu1 and Lu2 [15] (Fig. 11). The Lu1 site is sevenfold coordinated by oxygen atoms, forming a pentagonal bipyramid geometry, whereas the Lu2 site is sixfold coordinated, forming an octahedral structure. Structural studies on rare-earth-doped LSO report an average Lu1–O bond length of approximately 2.30 Å and the average Lu2–O bond length of about 2.21 Å. Owing to its higher coordination number and longer bond lengths, the Lu1 site is larger than the Lu2 site (see Fig. 1). The ionic radius of Ce^{3+} is 1.07 Å in sevenfold coordination and 1.01 Å in sixfold coordination, compared with 0.922 Å and 0.861 Å, respectively, for Lu^{3+} [25]. These values correspond to relative differences in ionic radii of ~ 16% for sevenfold coordination and ~ 17.3% for sixfold coordination, consistent with a strong preference of Ce^{3+} for substitution at the Lu1 site.

In bulk crystals with relatively high Ce^{3+} concentrations (0.2 - 1 at.%), approximately 95% of Ce^{3+} ions occupy the Lu1 site, while only about 5% substitute at the Lu2 site [16-17, 36]. The substantially different conditions employed for preparing LSO:Ce SCFs from low-temperature melt solutions, compared with crystals grown from high-temperature melts, can strongly influence the site-selective incorporation of dopant ions onto the host lattice. For LSO:Ce SCFs, this difference may be reflected in the relative probability of forming Ce1 and Ce2 centers. In particular, the formation of Ce1 centers appears to be more energetically favourable under low-temperature crystallization conditions than that of Ce2 centers. This behaviour is attributed to the substantially different volumes of the respective coordination polyhedra accommodating the relatively large Ce^{3+} ions, as well as their reduced thermal mobility during low temperature growth.

This assumption was recently supported by a study conducted by some of the present authors [37], which compared the optical and EPR properties of YSO:Ce SCFs with those of bulk single crystals. In that work, Ce2 centers were not detected by EPR measurements in the YSO:Ce films, indicating selective site occupation. A similar trend is expected for LSO:Ce SCFs. Consistently, the EPR measurements carried out in the present work on LSO:Ce SCFs also did not reveal Ce2 centers, further supporting the hypothesis that Ce^{3+} ions selectively occupy the Lu1 site under low-temperature growth conditions.

In LSO:Ce SCFs, preferential localization of Ce ions at the Lu1 site with sevenfold coordination is accompanied also by the incorporation of Pb^{2+} ions at the same positions, at concentrations comparable to that of cerium. This results in the formation of Ce^{4+}–Pb^{2+} pairs, which provide both local volume and charge compensation, as illustrated on the left-hand side of Eq. 2. As a consequence, many of the films listed in Table 1 do not exhibit Ce^{3+} EPR spectra.

The incorporation of Ce^{4+} ions is more complex, as the ionic radius of Ce^{4+} (0.87 Å) is sufficiently close to that of Lu^{3+} at both the Lu1 (0.922 Å) and Lu2 (0.861 Å) sites [25], suggesting that Ce^{4+} ions can, in principle, substitute for lutetium at either position. Therefore, accurately determining the site-specific distribution of Ce^{3+} and Ce^{4+} ions in LSO:Ce SCFs is of critical importance. Experimental confirmation of this distribution, at least for Ce^{3+} ions, can be effectively achieved through electron paramagnetic resonance spectroscopy. Although, Ce^{4+} is EPR-silent, annealing in a reducing atmosphere can convert Ce^{4+} to Ce^{3+}, allowing indirect determination of the Ce^{4+} location via EPR measurements. In particular, in a1 and b1 SCFs where Ce^{3+} spectra were clearly observed, Ce^{4+} ions are preferably substitute for Lu at the Lu1 sites.

The distribution of Ce^{3+}/Ce^{4+} ions and the presence of Pb^{2+} codopants strongly influence the optical and scintillation properties of as-grown LSO:Ce SCFs, compared to their bulk crystal counterparts (Figs. 5–7). Both LSO crystals and SCFs generally exhibit oxygen vacancies, which can act as charge-carrier trapping centers and adversely affect the scintillation figure of merit. The concentration of oxygen vacancies can be modified by high-temperature annealing in either oxidation or reducing atmospheres. In this context, thermal treatment plays a crucial role in altering the cerium valence state in LSO:Ce SCFs, thereby significantly impacting their optical and scintillation performance. Specifically, annealing in reducing or oxidizing atmospheres can shift the Ce^{4+}/Ce^{3+} equilibrium and modify the concentration of oxygen vacancies, which in turn affects luminescence intensity, afterglow behaviour, and overall scintillation efficiency.

A more detailed explanation of the possible effects of thermal treatment is as follows:

(i) Annealing in an oxidizing atmosphere. TT of LSO:Ce SCFs in an oxygen-rich environment (e.g., air) can reduce the concentration of oxygen vacancies and promote oxidation of Ce^{3+} to Ce^{4+} (see Eq. 1). While this process can decrease charge trapping and afterglow, the formation of Ce^{4+} may introduce alternative trapping centers, potentially reducing luminescence efficiency.

(ii) Annealing in reducing atmosphere (e.g., $N_2 + H_2$). In contrast, annealing in a reducing environment can promote the conversion of Ce^{4+} to Ce^{3+}, increasing the concentration of luminescent Ce^{3+} centers and enhancing LY and scintillation intensity (see Table 1). However, this treatment may also increase the number of oxygen vacancies, which can act as non-radiative recombination centers or prolong luminescence decay.

Due to the LPE growth of LSO:Ce SCFs from a PbO-based flux, we would also like to clarify the influence of the Pb^{2+} flux-related dopant on the structural, optical, and scintillation properties of these films. Specifically, the following key effects of Pb^{2+} incorporation are emphasized:

(i) Charge and volume compensation. Pb^{2+} ions substitute for Lu^{3+} predominantly at the Lu1 (seven-fold coordinated) sites, requiring local charge compensation. This strongly favours the formation of *Ce^{4+}–Pb^{2+} pair centers*, as supported by absorption spectra (O^{2-}→Ce^{4+} CTT bands) and the absence of Ce^{3+} EPR signals in as-grown and air-annealed films.

(ii) Modification of Ce valence equilibrium. The presence of Pb^{2+} stabilizes Ce^{4+} in the as-grown films. Thermal treatment in reducing atmosphere breaks Ce^{4+}–Pb^{2+} pairs and restores Ce^{3+}, which is directly confirmed by EPR and accompanied by enhanced Ce^{3+} luminescence and light yield.

(iii) Luminescence quenching and energy transfer. Pb-related centers introduce competing radiative and non-radiative recombination channels (Pb^{2+} intrinsic emission, Pb^{2+}–Pb^{2+} dimers, and exciton-related centers). These centers efficiently compete with Ce^{3+} for excitation energy, leading to reduced light yield and modified decay kinetics.

(iv) Influence on scintillation kinetics. Pb^{2+} codoping, together with other defects, alters charge carrier trapping and recombination pathways. This explains the reduced light yield, accelerated decay after air annealing, and slower decay after reduction TT, in agreement with previous reports on Pb-containing orthosilicate SCFs (Refs. [26, 27, 29]).

6. Conclusions

In this work, we report, for the first time, optical and EPR studies of the distribution and localization of Ce^{3+} ions in single crystalline films of Lu_2SiO_5:Ce orthosilicates, grown by liquid phase epitaxy on Y_2SiO_5 substrates. The measurements revealed the presence of only one type of Ce^{3+} center (Ce1), corresponding to the localization of Ce^{3+} ions in the 7–fold coordinated Lu positions of the Lu_2SiO_5 host. The determined g tensor parameters for Ce^{3+} ions in the films are consistent with those measured in bulk Lu_2SiO_5 crystals.

High-temperature annealing of the as grown films in air reduces the concentration of Ce^{3+} ions to a level undetectable by EPR due to the conversion of Ce^{3+} to the non-paramagnetic Ce^{4+} valence state, which is invisible in EPR. In contrast, thermal treatment in an $H_2 + N_2$ atmosphere significantly increases Ce^{3+} concentration (by a factor of three) due to the restoration of Ce^{3+} ions.

Our data also support the hypothesis that both Ce^{4+} and Ce^{3+} ions selective occupy only the Lu1 site in the films under low-temperature growth conditions.

The changes in the Ce valence induced by different thermal treatments also directly affect key scintillation parameters, such as luminescence intensity, decay time, and afterglow. However, overall scintillation efficiency depends on a delicate balance between Ce^{3+}/Ce^{4+} concentrations and defect formation during thermal treatment.

Acknowledgement

The support from Polish Nation Scientific Centre (NCN) Opus 24 No 2022/47/I/ST8/02600 project and Czech Science Foundation project no. 24-14580L is gratefully acknowledged.

References

(1) C.W.E. van Eijk, Inorganic-scintillator development. Nucl. Instr. Methods Phys. Res. A 460 (2001) 1-4. https://doi.org/10.1016/S0168-9002(00)01088-3.

(2) M. Nikl, A. Yoshikawa, Recent R&D Trends in Inorganic Single-Crystal Scintillator Materials for Radiation Detection. Adv. Opt. Mater. 3 (2015) 463-481. https://doi.org/10.1002/adom.201400571

(3) M. Nikl, V. V. Laguta, A. Vedda. Complex oxide scintillators: Material defects and scintillation performance**.** PSS (b) 245 (2008) 1701-1722. https://doi.org/10.1002/pssb.200844039

(4) O. Sidletskiy, A. Gektin, A. Belsky, Light-yield improvement trends in mixed scintillation crystals. PSS (a) 211 (2014) 2384-2387. https://doi.org/10.1002/pssa.201431137

(5) M. Globus, B. Grinyov, J. K. Kim, Inorganic Scintillators for Modern and Traditional Applications, ISC, Kharkiv, Ukraine, 2005.

(6) T. Martin, P.-A. Douissard, M. Couchaud, A. Cecilia, T. Baumbach, K. Dupre, A. Rack, LSO-Based Single Crystal Film Scintillator for Synchrotron-Based Hard X-Ray Micro-Imaging. IEEE TNS 56 (2009) 1412-1418. https://doi.org/10.1109/TNS.2009.2015878

(7)] A. Rack, S. Zabler, B.R. Mueller, H. Riesemeier, G. Weidemann, A. Lange, J. Goebbels, M. Hentschel, W. Goerner, High resolution synchrotron-based radiography and tomography using hard X-rays at the BAM*line* (BESSY II). Nucl. Instr. Methods Phys. Res. A 586 (2008) 327-344. https://doi.org/10.1016/j.nima.2007.11.020

(8) Y. Zorenko, V. Gorbenko, I. Konstankevych, T. Voznjak, V. Savchyn, M. Nikl, J. A. Mares, K. Nejezchleb, V. Mikhailin, V. Kolobanov, and D. Spassky. Peculiarities of luminescence and scintillation properties of YAP:Ce and LuAP:Ce single crystals and single crystalline films, Rad. Meas. 42 (2007) 528-532. https://doi.org/10.1016/j.radmeas.2007.01.046.

(9) P. Dorenbos, C.W.W. van Eijk, A.J.J. Bos, C. L. Melcher, Afterglow and thermoluminescence properties of Lu_2SiO_5:Ce scintillation crystals. J. Phys. Cond. Matter 6 (1994) 4167. https://doi.org/10.1088/0953-8984/6/22/016

(10) V. Laguta, M. Nikl, S. Zazubovich, Photothermally stimulated creation of electron and hole centers in Ce^{3+}-doped Y_2SiO_5 single crystals. Opt. Mat. 36 (2014) 1636-1641. https://doi.org/10.1016/j.optmat.2013.12.018

(11) Y. Zorenko, M. Nikl, V. Gorbenko, V. Savchyn, T. Voznyak, R. Kucerkova, O. Sidletskiy, B. Grynyov, A. Fedorov, Growth and luminescent properties of Lu_2SiO_5 and Lu_2SiO_5:Ce single crystalline films. Opt. Mat. 33 (2011) 846-852. https://doi.org/10.1016/j.optmat.2011.01.004.

(12) Yu. Zorenko, V. Gorbenko, V. Savchyn, T. Voznyak, V.V. Gorbenko, M. Nikl, J.A. Mares, O. Sidletskiy, B. Grynyov, A. Fedorov, K. Fabisiak, K. Paprocki, Opt. Mat. 34 (2012) 1969-1974. https://doi.org/10.1016/j.optmat.2011.11.021.

(13) Yu. Zorenko, V. Gorbenko, V. Savchyn, T. Voznyak, B. Grinyov, O. Sidletskiy, D. Kurtsev, A. Fedorov, V. Baumer, M. Nikl, J. A. Mares, A. Beitlerova, M. Kucera, Growth and luminescent properties of Lu_2SiO_5:Ce and $(Lu_{1-x}Gd_x)_2SiO_5$:Ce single crystalline films. J. Cryst. Growth 337 (2011) 72-80. https://doi.org/10.1016/j.jcrysgro.2011.10.003 .

(14) T. Karner, V. V. Laguta, M. Nikl, T. Shalapska, S. Zazubovich, On the origin of cerium-related centres in lead-containing single crystalline films of Y_2SiO_5:Ce and Lu_2SiO_5:Ce. J. Phys. D. Appl. Phys. 47(6) (2014), 065303. https://doi.org/10.1088/0022-3727/47/6/065303 .

(15) T. Gustafsson, M. Klintenberg, S. E. Derenzo, M. J. Weber, J.O. Thomas, Lu_2SiO_5 by single-crystal X-ray and neutron diffraction**.** Acta Cryst. C 57 (2001) 668-669. https://doi.org/10.1107/S0108270101005352.

(16) H. Feng, V. Jary, E. Mihokova, D. Ding, M. Nikl, G. Ren, H. Li, S. Pan, A. Beitlerova, R. Kucerkova, Temperature dependence of luminescence characteristics of scintillator grown by the Czochralski method. J. Appl. Phys. 108 (2010) 033519. https://doi.org/10.1063/1.3457856.

(17) I. N. Kurkin, K. P. Chernov, EPR and spin-lattice relaxation of rare-earth activated centres in Y_2SiO_5 single crystals. Physica 101B (1980) 233-238. https://doi.org/10.1016/0378-4363(80)90107-2

(18) L. Pidol, O. Guilott-Noël, A. Kahn-Harari, B. Viana, D. Pelenc, D. Gourier, EPR study of Ce^{3+} ions in lutetium silicate scintillators $Lu_2Si_2O_7$ and Lu_2SiO_5. J. Phys. Chem. Solids 67 (2006) 643-650. https://doi.org/10.1016/j.jpcs.2005.10.175

(19) M. Buryi, V. Laguta, D. Savchenko, M. Nikl.Electron Paramagnetic Resonance Study of Lu_2SiO_5 and Y_2SiO_5 Scintillators Doped by Cerium. Adv. Sci. Eng. Med. 5 (2013) 573-576. https://doi.org/10.1166/asem.2013.1319

(20) M. Buryi, V. Laguta, M. Nikl, J. Rosa, Electron paramagnetic resonance study of exchange coupled Ce^{3+} ions in Lu_2SiO_5 single crystal scintillator. Radiat. Meas. 90 (2016) 23-26. https://doi.org/10.1016/j.radmeas.2016.01.008

(21) M. W. Blair, B. L. Bennett, S. C. Tornga, N. A. Smith, R. E. Muenchausen, Reduced dimensionality effects on phonon transport. J. Appl. Phys. 108 (2010), 104311. https://doi.org/10.1063/1.3510533.

(22) Yu Zorenko, V. Gorbenko, V. Savchyn, T. Zorenko, B. Grinyov, O. Sidletskiy, A. Fedorov, Growth and luminescent properties of Ce and Ce–Tb doped $(Y,Lu,Gd)_2SiO_5$:Ce single crystalline films. J. Cryst. Growth 401 (2014) 577-583. https://doi.org/10.1016/j.jcrysgro.2014.01.066.

(23) Yu. Zorenko, V. Gorbenko, T. Zorenko, T. Voznyak, V. Vistovskiy, A. Voloshynovskii, K. Paprocki, L. Mosinska, P. Bilski, A. Twardak, A. Fedorov, M. Nikl, J.A. Mares, Luminescent and scintillation properties of $Sc^{3+}$and La^{3+} doped Y_2SiO_5 powders and single crystalline films. J. Lumin. 179 (2016) 445-450. https://doi.org/10.1016/j.jlumin.2016.07.039.

(24) URL**:** https://next-gen.materialsproject.org/materials/mp-3520/. Date accessed: December 10, 2025.

(25) URL**:** https://next-gen.materialsproject.org/materials/mp-16969. Date accessed: December 10, 2025.

(26) V. Gorbenko, A. Krasnikov, E. Mihokova, M. Nikl, S.Zazubovich, Yu. Zorenko, Luminescence of lead-related centers in single crystalline films of Lu_2SiO_5. J. Phys. D. Appl. Phys. 45 (2012) 355304. https://doi.org/10.1088/0022-3727/45/35/355304

(27) S. Zazubovich, A. Krasnikov, Yu. Zorenko, V. Gorbenko, V. Babin, E. Mihokova, and M. Nikl, Luminescence of Pb- and Bi-Related Centers in Aluminum Garnet, Perovskite, and Orthosilicate Single-Crystalline Films. In monography "Nanocomposite, Ceramic, and Thin Film Scintillators", p. 227-287. Published by Pan Stanford Publishing Pte. Ltd., USA. November 11, 2016. – 350 p.

(28) G. B. Scott, J. L. Page, Pb valence in iron garnets, J. Appl. Phys. 48 (1977) 1342-1349. https://doi.org/ 10.1063/1.323728.

(29) Yu. Zorenko, V. Gorbenko, V. Savchyn, T. Voznyak, O. Sidletskiy, B. Grinyov, M. Nikl, J. A. Mares, T. Martin, P. A. Douissard, Single crystalline film scintillators based on the orthosilicate, perovskite and garnet compounds, IEEE Trans. Nucl. Sci. 59 (2012) 2260-2268. https://doi.org/10.1109/TNS.2012.2188907

(30) Yu. Zorenko, V. Gorbenko, V. Savchyn, T. Zorenko, B. Grinyov, O. Sidletskiy, A. Fedorov, J. A. Mares, M. Nikl, M. Kucera, Lu_2SiO_5:Ce and Y_2SiO_5:Ce single crystals and single crystalline film scintillators: comparison of the luminescent and scintillation properties, Radiation Measurements, 56 (2013) 84–89. https://doi.org/10.1016/j.radmeas.2013.05.004.

(31) Zorenko Yu., Konstankevych I., Gorbenko V., Zorenko T. Growth and characteristics of crystallophosphors on the base of single crystalline films of LuAG and YAG garnets. Molecular Physics Reports. 36 (2002) 127-132. https://inis.iaea.org/records/4f00p-46g19

(32) Yu. Zorenko, J. A. Mares, P. Prusa, M. Nikl, V. Gorbenko, V. Savchyn, R. Kucerkova, K. Nejezchleb. Luminescence and scintillation characteristics of YAG:Ce single crystalline films and single crystals. Radiation Measurements. 45 (2010) 389–391. https://doi.org/10.1016/j.radmeas.2009.09.009

(33) U.S. Patent No. 8,278,624. Cerium activated lutetium oxyorthosilicate scintillator having a short decay time and method of making the same. Inventors: Merry A. Koschan, Charles L. Melcher, Piotr Szupryczynski, A. Andrew Carey. Filed: Aug 21, 2007. Date of Patent: Oct. 2, 2012. Patent Publication Number: 20110260107; https://patents.justia.com/patent/8278624

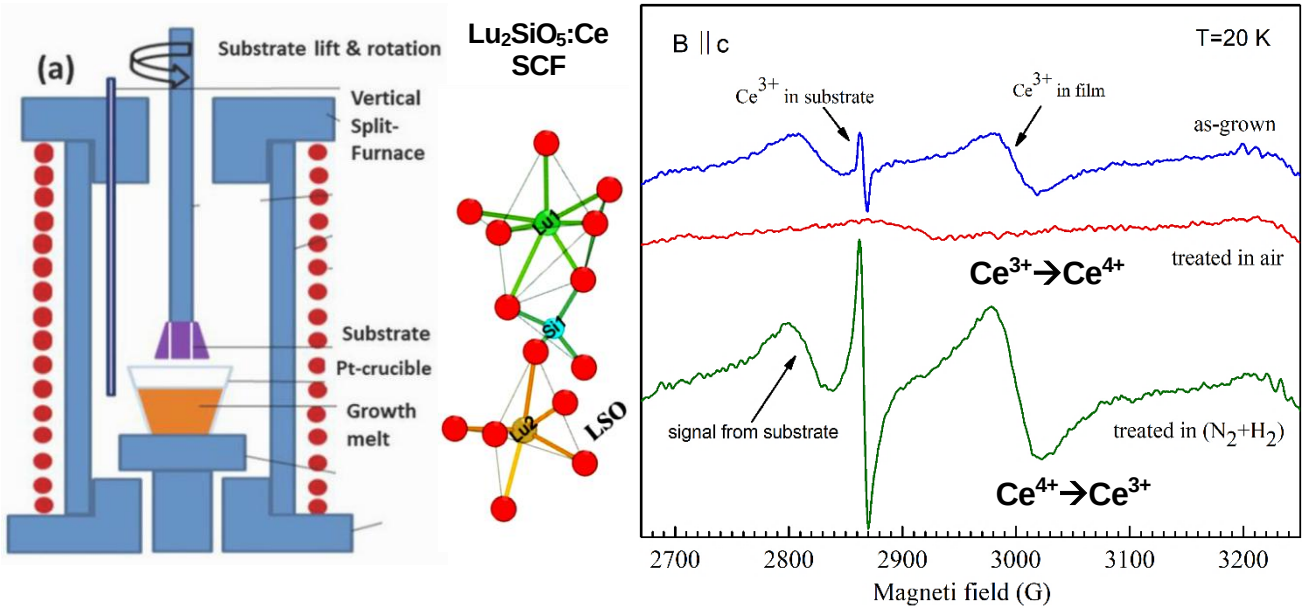
(34) Yang, K., Melcher, C. L., & Eriksson, L. Optical absorption and scintillation characteristics of LYSO:Ce and LYSO:Ce co-doped with Ca and Mg. IEEE Transactions on Nuclear Science, 60(2) (2013) 969–973. https://doi.org/10.1109/TNS.2013.2251995

(35) P.W. Anderson and P. R. Weiss, Exchange Narrowing in Paramagnetic Resonance. Rev. Mod. Phys. **2**5 (1953) 269. https://doi.org/10.1103/RevModPhys.25.269

(36) V. Babin, V. Laguta, M. Nikl, J. Pejchal, A. Yoshikawa, S. Zazubovich, On the luminescence origin in Y_2SiO_5:Ce and Lu_2SiO_5:Ce single crystals, Opt. Mat. 103 (2020) 109832. https://doi.org/10.1016/j.optmat.2020.109832 .

(37) V. Laguta, Yu. Zorenko, M. Buryi, V. Gorbenko, T. Zorenko, M. Nikl, EPR study of Ce^{3+} luminescent centers in the Y_2SiO_5 single crystalline films, Optical Materials, 72 (2017) 833-837. https://doi.org/10.1016/j.optmat.2017.09.035.

TOC figure


(a)
Substrate lift & rotation
Vertical
Split-
Furnace
Substrate
Pt-crucible
Growth
melt
Lu2SiO5:Ce
SCF
Lu1
Si
Lu2
LSO
B || c
T=20 K
Ce3+ in substrate
Ce3+ in film
as-grown
Ce3+→Ce4+
treated in air
signal from substrate
treated in (N2+H2)
Ce4+→Ce3+
2700
2800
2900
3000
3100
3200
Magneti field (G)